Weierstraß-Institut
für Angewandte Analysis und Stochastik

Leibniz-Institut im Forschungsverbund Berlin e. V.

Preprint ISSN 2198-5855

Simulating the electronic properties of semiconductor nanostructures using multiband $\mathbf{k} \cdot \mathbf{p}$ models

Oliver Marquardt

submitted: October 6, 2020

Weierstrass Institute
Mohrenstr. 39
10117 Berlin
Germany
E-Mail: oliver.marquardt@wias-berlin.de

No. 2773
Berlin 2020

2010 *Physics and Astronomy Classification Scheme.* 71.15.-m, 02.70.-c, 81.07.Gf.

Key words and phrases. Nanowires, quantum dots, electronic properties, $\mathbf{k} \cdot \mathbf{p}$ models.

O.M. was funded by the Deutsche Forschungsgemeinschaft (DFG, German Research Foundation) under Germany's Excellence Strategy - EXC2046: MATH+ Berlin Mathematics Research Center (project AA2-5).

Edited by
Weierstraß-Institut für Angewandte Analysis und Stochastik (WIAS)
Leibniz-Institut im Forschungsverbund Berlin e. V.
Mohrenstraße 39
10117 Berlin
Germany

Fax: +49 30 20372-303
E-Mail: preprint@wias-berlin.de
World Wide Web: http://www.wias-berlin.de/

Simulating the electronic properties of semiconductor nanostructures using multiband $\mathbf{k} \cdot \mathbf{p}$ models

Oliver Marquardt

Abstract

The eight-band $\mathbf{k} \cdot \mathbf{p}$ formalism been successfully applied to compute the electronic properties of a wide range of semiconductor nanostructures in the past and can be considered the backbone of modern semiconductor heterostructure modelling. However, emerging novel material systems and heterostructure fabrication techniques raise questions that cannot be answered using this well-established formalism, due to its intrinsic limitations. The present article reviews recent studies on the calculation of electronic properties of semiconductor nanostructures using a generalized multiband $\mathbf{k} \cdot \mathbf{p}$ approach that allows both the application of the eight-band model as well as more sophisticated approaches for novel material systems and heterostructures.

1 Introduction

Semiconductor nanostructures such as thin films [51, 68], nanowires (NWs) [38, 41, 40], quantum dots (QDs) [14, 13, 76], but also nanoparticles [34] or crystal-phase heterostructures [5, 24] represent key building blocks of novel optoelectronic devices. Within the past years, significant progress has been achieved in the production process of such nanostructures for applications in light emission and detection, solar energy harvesting, but also for single-photon generation techniques to be used in quantum communication or quantum computing [35, 77, 17, 31, 37].

Powerful modelling techniques for the investigation of the optoelectronic properties of semiconductor nanostructures are essential to both a deeper understanding of observations in experiment and to the design of nanostructures that suit the demands of very specific applications. A wide variety of modelling approaches exists for individual semiconductor nanostructures. Atomistic models, such as tight-binding [57, 59, 60] or empirical pseudopotential approaches [69, 70, 12] grant the flexibility to model nanostructures on the level of single atoms. [11, 73] However, the computational effort rapidly grows with the number of atoms involved. While the treatment of a few million atoms (as an orientation to the reader, in the common compound semiconductor material GaAs, one million atoms corresponds to a volume of approx. $35 \times 35 \times 35$ nm^3) in such models is nowadays possible [20, 4], these highly accurate atomistic models commonly require the availability of high-performance computer facilities with several hours to a few days of computational effort for a single nanostructure.

A computationally efficient alternative are $\mathbf{k} \cdot \mathbf{p}$ models that provide relevant details of the bulk electronic band structure of all materials involved in combination with an envelope function approach containing shape and dimensions of a heterostructure [8, 18]. In particular, the eight-band $\mathbf{k} \cdot \mathbf{p}$ formalism [7, 22, 54, 64, 6] represents the backbone of modern device modelling for the past two decades now and continues to provide valuable insight for recent research questions [29, 1, 30, 39]. Even today, eight-band $\mathbf{k} \cdot \mathbf{p}$ models are actively being researched and improved in terms of accuracy and applicability [66, 55]. While these models naturally neglect atomistic features and appear therefore unsuited to heterostructures where the influence of individual atoms governs the electronic properties,

DOI 10.20347/WIAS.PREPRINT.2773 Berlin 2020

they are extremely useful to identify and understand trends in classes of heterostructures, such as the influence of alloy composition, shape, or size of a set of heterostructures on their electronic properties. Despite being a reliable and efficient tool for the description of the electronic properties of semiconductor nanostructures, the eight-band $\mathbf{k} \cdot \mathbf{p}$ formalism has a number of shortcomings and limitations that are intrinsic to both the continuum framework as well as the limitation to eight basis functions.

The following work reviews our recent studies that have been performed using both the eight-band model as well as modifications of this model and more sophisticated $\mathbf{k} \cdot \mathbf{p}$ models. The intrinsic limitations of the eight-band $\mathbf{k} \cdot \mathbf{p}$ formalism together with approaches to handle them will be discussed in detail with a focus on semiconductor nanowires. This particular class of heterostructures exhibits unique features due to the existence of free side facets. These do not only facilitate a significant strain relaxation that allows the development of defect-free heterostructures, but also the coexistence of different crystal phases of chemically identical composition. In the following, the application of $\mathbf{k} \cdot \mathbf{p}$ models to investigate the electronic properties of of nanowire-based heterostructures defined by chemical composition or crystal phase will be reviewed.

2 Generalized multiband $\mathbf{k} \cdot \mathbf{p}$ models

Within $\mathbf{k} \cdot \mathbf{p}$ perturbation theory, the bulk electronic band structure of a semiconductor material is described for a limited number of basis functions (bands) in the vicinity of a selected high-symmetry point of the Brillouin zone [28]. The relevant optically active transitions in a semiconductor quantum dots commonly rely on electron and hole states that are dominated by the energetically lowest conduction band and the top valence bands, respectively, in the vicinity of high-symmetry points. In direct semiconductors such as most compound semiconductors of the III-As and III-N material systems, the minimum of the conduction band and the maximum of the valence band appear at the same high-symmetry point, which in this material class is commonly $\Gamma = \mathbf{k} = \mathbf{0}$. The eight-band $\mathbf{k} \cdot \mathbf{p}$ formalism therefore treats the three energetically highest valence bands and the energetically lowest conduction band each with their respective spin components, spin-up ($|\uparrow\rangle$) and spin-down ($|\downarrow\rangle$), assuming that other bands are energetically well separated from this basis set (cf. Fig. 1). The corresponding Hamiltonian is a matrix with the row and column indices $\sigma, \nu = 1, 2, ..., 8$:

$$\hat{H} := \sum_{\sigma,\nu} |\sigma, \mathbf{r}\rangle \hat{H}_{\sigma\nu}(\mathbf{r}) \langle \nu, \mathbf{r}|. \tag{1}$$

Each of the elements $\hat{H}_{\sigma\nu}$ is a sum of terms, that are composed as a product of up to four factors

$$c \cdot P(\mathbf{r}) \cdot \phi(\mathbf{r}) \cdot \hat{D}. \tag{2}$$

Here, c represents a real or imaginary prefactor. $P(\mathbf{r})$ is a spatially dependent parameter, such as an effective mass or the Luttinger parameters. The quantities $\phi(\mathbf{r})$ are additional fields such as the spatially dependent elements of the strain tensor and polarization or other external potentials. $\hat{D}$ represents gradient operators (commonly first and second spatial derivatives). The respective material parameters can be mostly deduced from band curvature, optical selection rules, and symmetry considerations so that only a handful of material parameters such as effective masses, band edges, or optical matrix elements, is required to provide a reasonable approximation of the band structure of a material around the Γ point using the eight-band $\mathbf{k} \cdot \mathbf{p}$ model. The actual composition and geometry of heterostructures is then encoded in spatially dependent material parameters. In ternary or quaternary alloys, material parameters are interpolated using linear or quadratic interpolation schemes, according to the material composition at the respective position. For the common compound semiconductors,

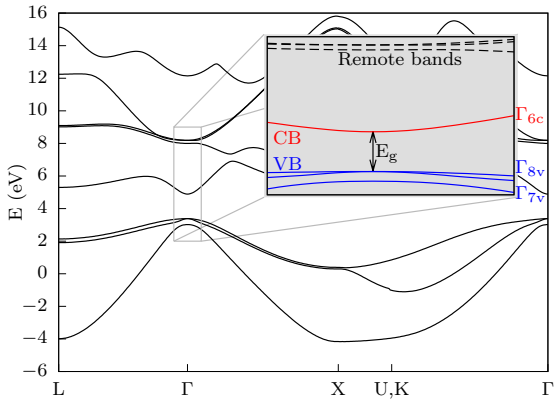

Figure 1: Band structure of GaAs. The magnification shows the basis functions of the eight-band $\mathbf{k}\cdot\mathbf{p}$ formalism around $\Gamma = \mathbf{0}$. The conduction band is depicted in red, the valence bands are shown in blue. Some remote bands that are part of the bulk band structure but not of the eight-band $\mathbf{k}\cdot\mathbf{p}$ model are shown additionally (dashed black).

eight-band $\mathbf{k}\cdot\mathbf{p}$ parameters are well known and can be found in literature (e.g. Ref. [67]). The bulk band structures are furthermore modified by strain and built-in electrostatic potentials that commonly arise in epitaxially-grown semiconductor heterostructures. Eight-band models taking these effects into account can be found e.g. in Refs. [7, 22], or [71].

We have previously developed a flexible, generalized multiband $\mathbf{k}\cdot\mathbf{p}$ formalism within the plane-wave framework of the SPHInX library [42, 16, 43]. In this manner, we could apply highly optimized electronic minimization routines that were readily available, and perform highly efficient gradient operations in reciprocal space, where the real-space properties of heterostructures are transformed via Fast Fourier Transformation. The key feature of our implementation, however, is a generalized Hamiltonian which is set up in a human-readable meta-language. In particular, the dimensions of the Hamiltonian and thus the number of bands taken into account is not limited so that the code grants the flexibility to perform not only eight-band $\mathbf{k}\cdot\mathbf{p}$ calculations but also computationally inexpensive single-band effective mass simulations as well as more sophisticated models beyond the eight-band scheme, as will be discussed in Sec. 6.

The typical work flow of a simulation is depicted in Fig. 2. The heterostructure is set up in a 3D material map containing shape and material composition. The respective material parameters are read from separate material parameter files. In the first step, the elastic properties of the system are then computed using a continuum elasticity model that is part of the software [43]. Built-in electrostatic potentials are computed from strain distribution, piezoelectric constants, and spontaneous polarization by solving the Poisson equation. These contributions enter the generalized multiband $\mathbf{k}\cdot\mathbf{p}$ model, where the respective $\mathbf{k}\cdot\mathbf{p}$ Hamiltonian is chosen and set up by the user such that it suits best the complexity of the underlying problem. The resulting single-particle wave functions, charge densities, and energies can then be used in an external self-consistent cycle to account for excitonic effects and thus to compute optical spectra of the heterostructure under consideration. Of course, parts of the simulation work flow can be replaced by other software packages (e.g. more detailed elasticity models)

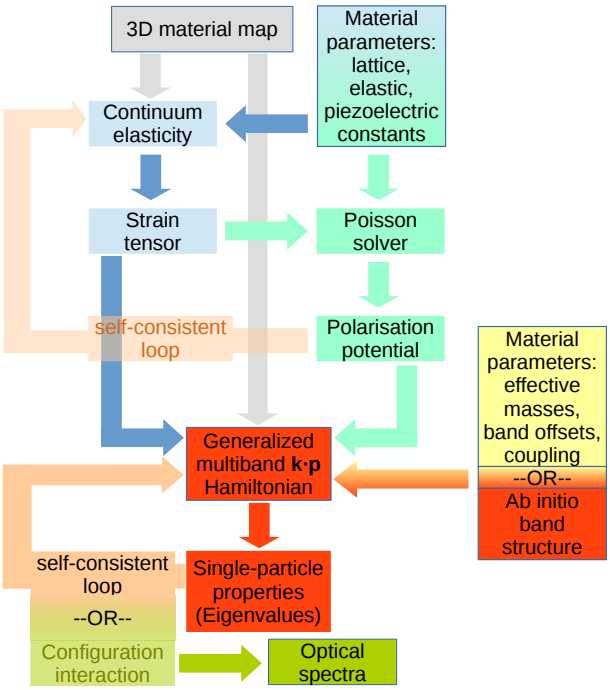

Figure 2: Schematic of the simulation work flow. The self-consistent coupling between the calculation of elastic and piezoelectric properties as well as the configuration interaction scheme are realized by scripts outside the SPHInX $\mathbf{k} \cdot \mathbf{p}$ module to allow for maximum flexibility.

following a simple grid interpolation. High numerical efficiency, flexibility, and the widely generalized approach of the SPHInX multiband $\mathbf{k} \cdot \mathbf{p}$ module allowed us to compute the electronic properties of a wide range of semiconductor nanostructures, some of which will be presented in more detail in the following.

3 Random dopant fluctations and surface potentials in (In,Ga)N nanowires

$In_xGa_{1-x}N$/GaN heterostructures are key building blocks for highly efficient, environmentally friendly white light-emitting diodes, as the band gap of the ternary alloy $In_xGa_{1-x}N$ spans a spectral range from 380 to 1800 nm, thus covering the entire visible spectrum [51]. However, it is generally difficult to synthesize $In_xGa_{1-x}N$/GaN heterostructures with large In contents, as required for light emission in the yellow, amber, and red part of the spectrum. A large lattice mismatch as well as the tendency of phase separation represent severe obstacles in the production of $In_xGa_{1-x}N$ layers in GaN with large In contents while maintaining the required crystal quality. Moreover, $In_xGa_{1-x}N$/GaN heterostructures exhibit large built-in potentials that increase linearly with In content and layer thickness. These potentials induce a spatial separation of electrons and holes and therefore significantly reduce the efficiency of radiative recombination [75]. Both problems can be overcome by incorporating $In_xGa_{1-x}N$ layers in GaN nanowires [38, 40] where the free side facets facilitate strain relaxation so that axial $In_xGa_{1-x}N$ layers can relax elastically even for large In contents [15, 33]. At the same time, the elastic strain release is expected to reduce the built-in electrostatic fields and thus to increase the electron-hole overlap, leading to an increased internal quantum efficiency [68]. Surprisingly, the emission wavelengths observed in axial $In_xGa_{1-x}N$/GaN nanowires were all reported in the green, amber, and red parts of

the spectrum and furthermore decrease monotonically with decreasing In content so that emission within the blue or violet parts of the spectrum becomes difficult (cf. Fig. 3 a) [72]. This behavior is, in fact, the opposite of what is regularly observed in planar $In_xGa_{1-x}N$/GaN heterostructures.

The fundamental difference between planar heterostructures and those incorporated in nanowires are the free side facets and thus the presence of surface potentials in semiconductor nanowires. These potentials arise from surface Fermi level pinning at the semiconductor-vacuum interface and background doping throughout the whole nanowire [19]. In a first step, we have thus performed a systematic study of the influence of the In x content on the confinement of electrons and holes in an axial $In_xGa_{1-x}N$/GaN nanowire heterostructure, taking a surface potential into account [47]. The doping concentration inside the nanowire was modelled in a simplified assumption as a homogeneous background charge, giving rise to a parabolic increase of the surface potential towards the side facets. We have identified the competing influence of strain-induced built-in polarization potentials and surface potentials arising from unintentional doping and surface Fermi level pinning as the origin of the counterintuitive emission properties of axial $In_xGa_{1-x}N$/GaN nanowire heterostructures. While the surface potential exhibits its maximum at the side facets of the nanowire, the built-in polarization potential has its maximum at the bottom interface of the $In_xGa_{1-x}N$ insertion along the central axis of the nanowire (cf. Fig. 3 b). Assuming the surface potential to be indepentent of the In content and thus constant for all x, the strength of the polarization potential increases with larger In content. The valence band maximum – the attractive area for hole states – moves from the side facets towards the central axis of the nanowire with larger In contents so that hole states are confined near the side facets for small In contents and near the central axis of the nanowire for larger In contents, where their overlap with the electron state (always located at the central axis of the nanowire and the top interface if the $In_xGa_{1-x}N$ insertion) is larger (cf. Fig. 3 c).

To reduce the disturbing influence of surface potentials for nanowire-based light emission in the blue and violet range, a reduction of the nanowire diameter was found to be a promising approach. First, the surface potential increases quadratically with the nanowire diameter so that a reduction within experimentally accessible ranges (e.g. from 80 to 40 nm) reduces the strength of the surface potential by a factor of four. Second, confining electrons and holes on a smaller volume itself leads to an increased overlap and thus higher internal quantum efficiency [45]. However, given the dimensions of these nanowires, a typical density of unintentional doping of p=10^{-17}cm^{-3} as assumed in the above study with a nanowire diameter of 40 nm translates into only two dopants in a 20 nm long segment of a nanowire, a density where the approximation of a homogeneous doping density naturally fails [36, 58, 26].

Motivated by this consideration, we have studied the influence of individual, randomly distributed dopants in axial $In_xGa_{1-x}N$/GaN nanowire heterostructures on their electronic properties [46]. Doping is clearly an atomistic feature and thus at a first glance not tractable within a continuum picture. However, we know that typical unintentionally incorporated dopants in the (In,Ga)N material system are O and Si donors [23, 19, 26] that transfer their extra electron to surface states in the vicinity of a semiconductor-vacuum interface, which basically applies to all donors in a nanowire. Furthermore, it is known that O and Si represent almost ideal hydrogenic donors in the (In,Ga)N material system [50] so that their main influence is a long-range Coulomb potential. We have therefore modelled random donor distributions in axial $In_xGa_{1-x}N$/GaN using single point charges that contribute a Coulomb potential to the potential landscape within an eight-band $\mathbf{k}\cdot\mathbf{p}$ model. An example of a Coulomb potential as well as the corresponding electron and hole ground state charge density is shown in Fig. 3 d, where nine randomly distributed donors are contained in an $In_{0.05}Ga_{0.95}N$ insertion of 1 nm thickness in a GaN nanowire. We have then performed a statistical analysis for selected systems in terms of In content and insertion thickness, where we have simulated 500 random doping distributions for each – other-

wise identical – system configuration. The transition energy between electron and hole ground state is shown as a histogram for one example system configuration of In content and layer thickness (x=0.05, t=1 nm) in Fig. 3 e. It can be seen that fluctuations in the donor distribution alone lead to variations of more than 100 meV in the transition energy. Furthermore, the transition energies are mostly lower than those obtained under the assumption of a homogeneous doping charge density, as the potential valleys induced by individual donors are deeper (solid red line) and, of course, smaller than in the absence of a surface potential (dashed black line). While the position of the hole ground state can be predicted to be at one of the corners at the lower interface of the insertion, the electron confinement is mainly governed by the doping distribution, as can be seen in Fig. 3 f, where an ensemble charge density of electrons and holes for 500 different doping distributions is shown. The only reliable prediction for the electron is that it will be confined somewhere at the top interface of the insertion, due to the built-in polarization potential.

Random dopant fluctuations will therefore have a dramatic influence on nanowire applications that rely on the reproducible emission of light, such as single-photon emitters as required for quantum computing or -cryptography. Generally, the miniaturization of light emitters to the nanoscale will result in phenomena related to random doping fluctuations that need to be taken into account in design and modelling. Note, however, that the assumption of a homogeneous doping charge distribution in semiconductor nanowires is not a priori wrong: for larger doping densities as well as in cases where the doped area is spatially separated from the optically active parts of the device (e.g. in core-shell nanowires), the Coulomb potential of random doping concentrations will be well approximated by the one originating from a homogeneous doping density.

4 Polytypism in GaAs nanowires

Another unique property of semiconductor nanowires is the coexistence of different crystal phases (polytypes) of chemically identical alloys in the same nanowire. This feature occurs regularly in semiconductor nanowires and as the electronic properties of different polytypes of the same alloy are different, such nanowires represent crystal-phase heterostructures [63, 74]. Of particular interest in this context is the binary alloy GaAs, which can be considered as the prototype compound semiconductor material, used in a wide range of electronic and optoelectronic applications [49]. While the material properties of the zincblende (ZB) phase of GaAs are extensively studied and known with higher accuracy than those of any other compound semiconductor [2, 67], its metastable wurtzite (WZ) phase is scarcely understood. This is mostly due to the fact that WZ GaAs is unattainable in bulk form. While WZ GaAs is regularly observed in nanowires, it always occurs only in coexistence with the ZB phase in a sequence of segments of alterating crystal phase and thickness. Extracting the bulk material properties of the WZ phase from polytypic GaAs nanowires is, of course, beset with many difficulties so that complete and consistent sets of electronic structure parameters of WZ GaAs are available only from theory [27, 10, 9]. Existing studies agree, however, that there are two energetically close conduction bands relevant for optoelectronic properties in the WZ phase. Apart from the Γ_{7c} band, the equivalent to the Γ_{6c} band of the ZB phase (cf. Fig. 4 a), the much heavier Γ_{8c} band coexists in close energetical range (cf. Fig. 4 b) and the ordering of the two bands is still matter of controverse discussion. Moreover, the ordering of the two bands can be reversed by even small strains [21, 61], of a magnitude that can already be imposed on dispersed nanowires by the substrate (cf. Fig. 4 c and d). This feature represents a challenge for the modelling of the electronic structure of GaAs crystal-phase heterostructures using $\mathbf{k} \cdot \mathbf{p}$ models as the Γ_{8c} conduction band is simply not contained in the eight basis functions. A proper model thus has to contain the additional conduction band, as can be done in

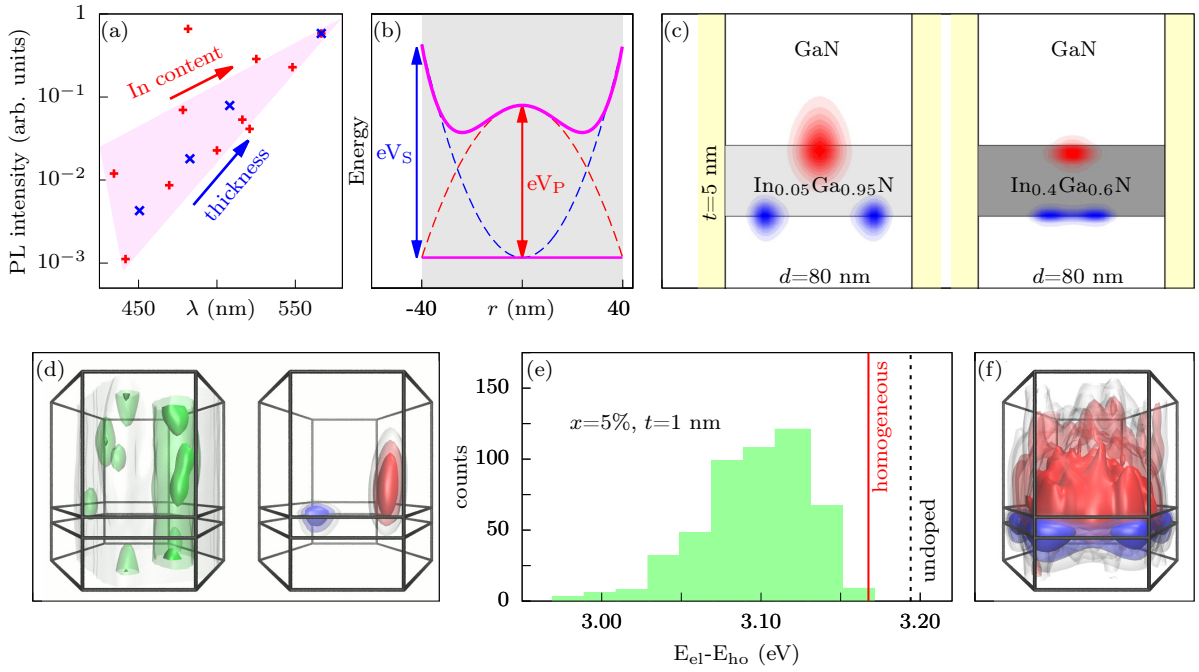

Figure 3: a: Photoluminescence intensity as a function of the peak emission wavelength for samples with different In contents (red '+') and thicknesses (blue '×'). b: Schematic plot of the influence of polarization (red) and surface potential (blue) on the valence band (solid purple). The unmodified valence band is shown as a thin purple line. c: Electron (red) and hole (blue) ground state charge densities for In contents of 5 and 40% in the active layer in a side-view. d: Coulomb potential (green) as well as electron (red) and hole (blue) ground state charge density in an axial $In_{0.05}Ga_{0.95}N$/GaN nanowire heterostructure arising from nine randomly distributed, ionized dopants. Isosurfaces represent 25, 50, and 75% of the extrema of potential and charge densities. The thickness of the active layer is 1 nm. e: Transition energy histogram over 500 random dopant distributions for $x = 0.05$ and t=1 nm. The solid red line indicates the transition energy assuming a homogeneous doping charge density, the dashed black one the one in the absence of doping. f: ensemble average of electron (red) and hole (blue) charge densities for 500 different doping distributions for $x = 0.05$ and t=1 nm.

a straightforward manner within the generalized SPHInX multiband $\mathbf{k} \cdot \mathbf{p}$ module.

Correspondingly, we have employed a ten-band $\mathbf{k} \cdot \mathbf{p}$ model to compute the electronic properties of GaAs crystal-phase heterostructures consisting of both ZB and WZ segments [48]. We have simulated both bulk nanowire segments consisting of one of the two polytypes as well as ZB/WZ superlattices under the influence of strain. Our calculations have shown that, in WZ GaAs, electron confinement can be governed by either the Γ_{7c} or the heavier Γ_{8c} band, which exhibits much lower recombination rates with hole states that are furthermore sensitive to light polarisation. In ZB/WZ superlattices, our findings indicate that, due to the two conduction bands in the WZ phase and the low band offset between the conduction bands of the two polytypes, electron confinement can appear in both the ZB or the WZ phase, depending on strain state and the thickness of the respective layers, whereas the hole ground state is always found to be confined in the WZ segment (cf. Fig. 4 e and f). As there is no coupling between the two conduction bands, the change of character of the electron ground state between $\Gamma_{6c,7c}$ and Γ_{8c} and the confinement region between ZB and WZ segment happens abrupt, as can be seen in Fig. 4 g. The WZ region dominates electron confinement if the ZB segments are thin enough that quantum confinement increases the energy of electrons in the ZB above the energy of an electron confined in the WZ region. The Γ_{8c} band is furthermore decreased in energy with increasing strain so that electron confinement due to this band again becomes dominant in the WZ phase for larger strains.

Apparently, any model of the electronic properties of heterostructures containing GaAs in the WZ phase strictly requires the consideration of the additional Γ_{8c} conduction band. The significant influence of comparatively small strains on the character of the electron ground state is a possible explanation for the contradicting experimental results regarding character and effective mass of the lowest conduction band in WZ GaAs and the corresponding band gap.

5 Excitonic Aharonov-Bohm effect in crystal-phase quantum rings based on core-shell nanowires

In radial core-shell nanowire heterostructures, polytypes extend through the shells during radial growth. This feature allows to combine radial, compositional core-shell nanowire heterostructures with axial crystal-phase heterostructures in order to form thin crystal-phase quantum rings. A clear advantage of heterostructures that are formed by alterations of the crystal phase rather than the chemical composition is the absence of interface grading between different alloys as well as the fact that crystal-phase heterostructures exhibit atomically flat interfaces and only a small lattice mismatch (for example, the lattice mismatch between the WZ and the ZB phase of GaAs is 0.37%). If such a nanowire-based crystal-phase quantum ring is furthermore supplied with a surface potential originating from intentional doping, electrons and holes can be confined inside the ring on different radii. A schematic realization of such a structure is shown in Fig. 5 a: An intentionally doped ZB GaAs core containing a single WZ segment is radially overgrown by an AlAs barrier shell, followed by the active, undoped GaAs shell and another AlAs barrier shell. The WZ segment extends radially through the whole nanowire, forming a ring inside the GaAs shell. The doped core supplies the whole nanowire with a surface potential so that electrons and holes are both confined in the WZ-GaAs ring but on different radii: The hole tends to be confined near the inner ring radius, the electron near the outer one. The slope of the surface potential can be controlled by the doping density of the core, p, the spatial separation between electrons and holes is limited by the experimentally well accessible shell thickness t. If such a radially polarized exiton is influenced by a magnetic field, the magnetic flux through the orbits defined by the electron

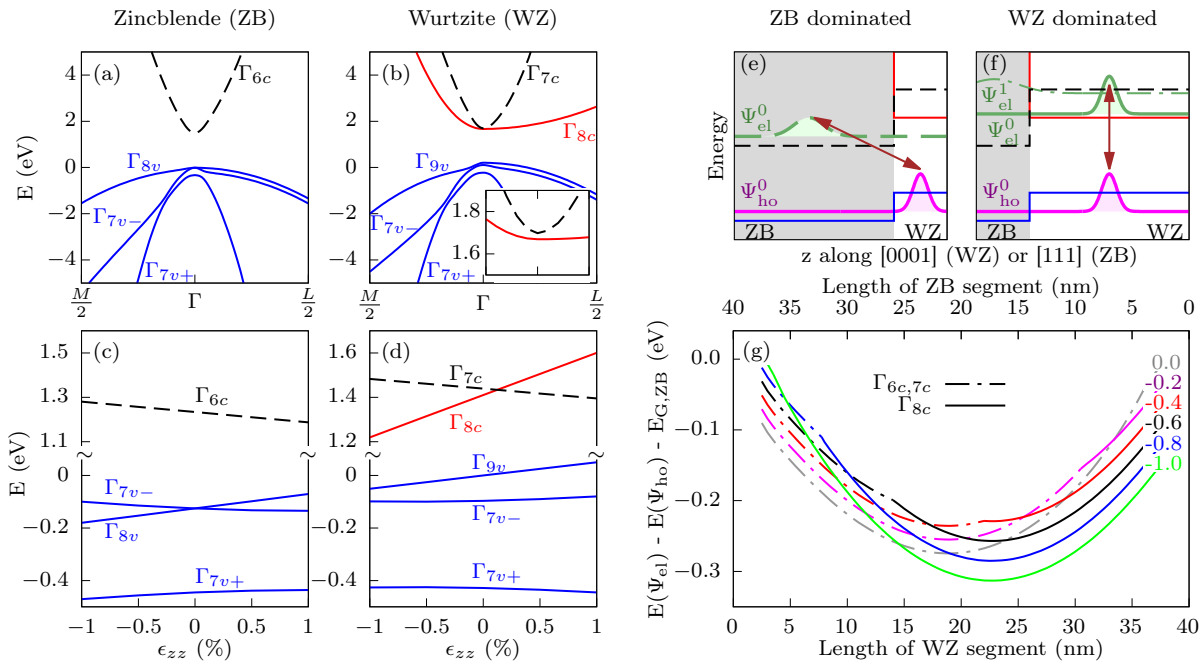

Figure 4: a and b: Bulk band structures of ZB and WZ GaAs. The inset in (b) shows a close-up of the conduction band minimum around Γ. c and d: Influence of strain on the band edges of ZB and WZ GaAs. e and f: Possible optical transitions in GaAs ZB-WZ superlattices. g: Transition energies relative to the ZB bulk band gap as a function of the thickness of the WZ and ZB segment for different strain states.

and the hole wave functions is different. Increasing the magnetic field then gives rise to oscillations in both the exciton energy and the oscillator strength characterized by a period B_C:

$$B_C = \frac{\Phi_0}{\pi \cdot |\langle r_e^2 \rangle - \langle r_h^2 \rangle|} \tag{3}$$

where $\Phi_0 = 2\pi - \hbar/e$ is the magnetic flux quantum. This effect is known as the excitonic Aharonov-Bohm effect [3, 56] and represents a fundamental quantum physical phenomenon. Crystal-phase quantum rings in all-binary semiconductor core-shell nanowires as suggested above represent promising structures for systematic studies of the excitonic Aharonov-Bohm effect, as the two characteristic parameters, the active shell thickness t and the core doping density p can be controlled to a good extent. The ideal case, however, represents a compromise between a radial separation of electron and hole large enough to warrant a small characteristic magnetic field B_C on the one hand and a sufficiently small separation to ensure visible recombination. We have therefore studied a range of experimentally realizable crystal-phase quantum rings in order to identify ideal systems for the observation of the excitonic Aharonov-Bohm effect in a recent work [25].

The GaAs core of the heterostructure (d_c=30 nm) is doped with Be at a doping density of 1 to 4×10^{18}, one order of magnitude larger than the doping level assumed in our study on axial $In_xGa_{1-x}N$/GaN nanowire heterostructures. As the core is furthermore separated from the active GaAs layer by a 15 nm thick AlAs shell, the simplification of a homogeneous core doping density appears reasonable. The crystal-phase segment realizing the axial confinement along the radial nanowire heterostructure is realized by a thin WZ segment in a merely ZB nanowire, namely a twin boundary. We could limit ourselves here to the consideration of only one conduction band (as contained in the eight-band $\mathbf{k}\cdot\mathbf{p}$ model, as our previous studies have shown that this is the dominating band in heterostructures

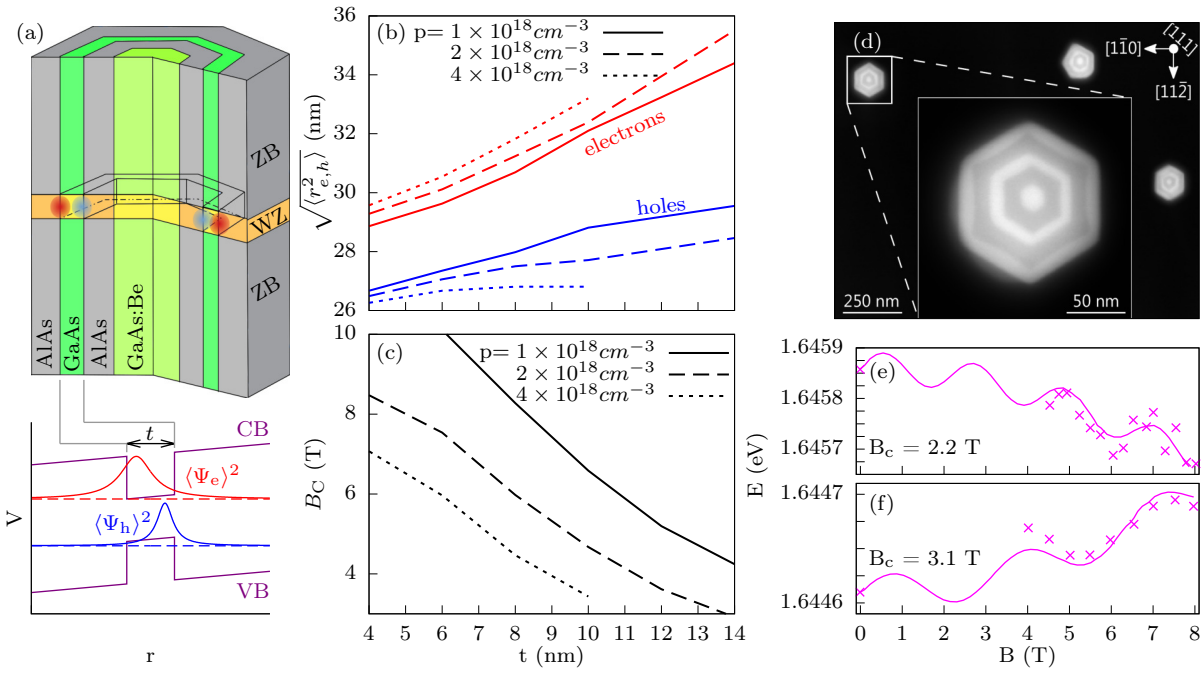

Figure 5: a: Schematic view of a GaAs/AlAs core-multishell nanowire with a Be-doped core containing a single twin boundary (WZ segment). The respective band profile of the active GaAs shell is shown below. Electron and hole ground state charge densities are depicted in red and blue, respectively. b: Electron (red) and hole (blue) radii as a function of the GaAs shell thickness t for different core doping densities p. c: Characteristic magnetic field B_{c} to achieve a phase shift of 2π of the exciton wavefunction as a function of t for different values of p. d: Plan-view high-angle annular dark-field transmission electron micrograph of a few GaAs/AlAs core-multishell nanowires with magnification of one selected nanowire. e and f: Dependence of the average energy of the Zeeman split states on the magnetic field for quantum rings from two different nanowires with the respective characteristic magnetic field B_{c}.

containing only thin WZ segments. We have then systematically varied both core doping density and GaAs shell thickness to obtain electron and hole ground state radii and the respective characteristic magnetic fields $\mathrm{B_C}$ to observe a 2π phase shift of the exciton wavefunction.

Figure 5 b shows electron and hole ground state radii as a function of the thickness of the active GaAs shell for different core doping densities. Clearly, both parameters are well suited to control the radial separation of the two charge carriers. The corresponding characteristic magnetic fields are shown in Fig. 5 c. The characteristic magnetic fields for the observation of a 2π phase shift of the exciton wavefunction can be tuned to less than 4 T for shell thicknesses that still allow visible optical recombination.

Following the theory-driven design, comparable nanowires were grown by molecular-beam epitaxy (for details on the growth procedure, see Ref. [25]). Example heterostructures are shown in a plan-view transmission electron microscopy image in Fig. 5 d with an enlarged view of one selected nanowire. The core-shell structure is clearly visible. Note that the nanowire is covered by another GaAs layer to prevent oxidation of the AlAs shell. Furthermore, a small number of twin boundaries was observed in each nanowire that represent the crystal-phase alterations required to achieve axial confinement of the charge carriers (not shown).

Magneto-photoluminescence spectroscopy was carried out on two selected, individual nanowires with

magnetic fields from 0 to 8 T. The transition energies of the two nanowires are shown in Figs. 5 e and f as a function of the magnetic field. The parabolic evolution of the transition energy, a result of the Zeeman effect, is clearly superimposed by oscillations. A fitting using a parabola modulated by a sine function yields characteristic magnetic fields of 2.2 and 3.1 T for the two nanowires. It is furthermore interesting to note that the underlying parabolic behaviour is of opposite direction in the two nanowires. This can be attributed to the fact that we observe Aharonov-Bohm oscillations for both a charged exciton, namely a trion (Fig. 5 e) and a neutral exciton (Fig. 5 f). We note that predicted and extracted characteristic magnetic fields deviate with a factor of approximately two, which is, however, not too surprising given the simplicity of the model employed and the number of uncertainties in measuring core doping levels and shell thicknesses. Our results demonstrate that crystal-phase quantum rings in GaAs/AlAs core-shell nanowires are ideal structures for systematic studies of the excitonic Aharonov-Bohm effect, offering a high degree of control over the two decisive characteristic parameters shell thickness and core doping density.

6 Beyond the eight-band scheme

While most of the above studies were based on eight-band $\mathbf{k}\cdot\mathbf{p}$ models, a fundamental shortcoming of this model, namely the limitation to eight basis functions, was already illustrated in the context of WZ GaAs, where a second, energetically close conduction band becomes relevant, so that the number of basis functions has to be extended. In a first study, this has been done by adding another conduction band, thus employing a ten-band Hamiltonian [48]. Given the fact that the only dipole-allowed transition between this band and any other of the basis functions involved (namely the $\Gamma_{9\mathrm{v}}$ valence band) is known to be very small [9], the additional conduction band has been modelled as a parabolic band, decoupled from all other basis functions. This model has successfully given valuable insight into the electronic properties of WZ/ZB GaAs heterostructures and provided useful information to the controversial debate on the nature of the lowest conduction bands in WZ GaAs and their influence on electron confinement and optical properties.

Limitations of the eight-band model Within the ten-band $\mathbf{k}\cdot\mathbf{p}$ model applied above, both conduction bands can be considered parabolic only in the very close vicinity of the Brillouin zone's center, Γ, and show additional band minima at other high-symmetry points that are energetically close to their energies at Γ. In order to achieve a more accurate description of the two conduction bands, more remote bands have to be taken into consideration. For WZ GaAs and GaAs crystal-phase heterostructures, we have therefore suggested to add the following three conduction bands to the ten-band model, again with their respective $|\uparrow\rangle$ $|\downarrow\rangle$ components, adding up to a 16-band $\mathbf{k}\cdot\mathbf{p}$ model.

Generally, a more accurate description of the band structure throughout wider parts of the Brillouin zone can be achieved by increasing the number of bands taken explicitly into account [32, 65, 43]. For example, the application of an eight-band $\mathbf{k}\cdot\mathbf{p}$ models to heterostructures with a fourfold symmetric geometry, e.g. pyramidal quantum dots in the ZB phase, induces artificially degenerate electronic states which would exhibit a small energy splitting in atomistic models. The origin of the splitting is the bulk-inversion anisotropy, which reduces the combined symmetry of atomistic lattice and heterostructure geometry, which is not contained in common eight-band $\mathbf{k}\cdot\mathbf{p}$ models [12]. Taking more bands into account, however, it is possible to provide a correct description of the bulk-inversion anisotropy even in a $\mathbf{k}\cdot\mathbf{p}$ model. As an example, the band structures reproduced from two-plus-six-, eight- and 14-band $\mathbf{k}\cdot\mathbf{p}$ models for ZB GaAs are shown in Fig. 6 a, where three more conduction bands were taken into account. Note that both conduction and valence bands exhibit small splittings towards the K high

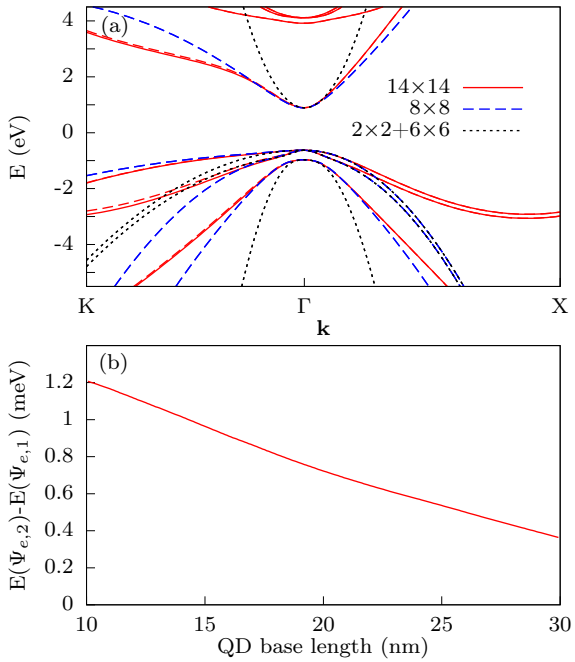

Figure 6: a: Electronic band structure of bulk ZB GaAs reproduced from effective mass and six-band (dotted black), an eight-band (dashed blue), and a 14-band (solid and dashed red) $\mathbf{k}\cdot\mathbf{p}$ model. b: energy splitting between the first two, p-like excited electron states in a pyramidal InAs quantum dot in GaAs as a function of the QD base length.

symmetry point for the 14-band model (dashed and solid red lines), a feature that is not resolved in the two less sophisticated models. Applying the same 14-band Hamiltonian [53] to an InAs pyramidal QD in GaAs, we can in fact observe a splitting between the two p-like excited electron states, which are found to be degenerate in the eight- or two-band models (cf. Fig 6 b where the splitting is shown as a function of the QD base lenght).

Parameter fitting The description of heterostructures formed from indirect band gap materials such as Si or Ge, compound semiconductors in metastable crystal phases, or 2D materials using $\mathbf{k}\cdot\mathbf{p}$ models will likewise require larger basis sets. While the respective Hamiltonian operators can be set up in a straight-forward manner within the SPHInX multiband $\mathbf{k}\cdot\mathbf{p}$ module, the set of required material parameters is another key ingredient and – opposed to the parameters required for eight-band models – not well known for most materials. Moreover, obtaining these parameters by fitting the respective $\mathbf{k}\cdot\mathbf{p}$ band structure to a band structure obtained from *ab initio* calculations becomes a nontrivial task if high accuracy throughout the whole Brillouin zone is demanded. For example, the common eight-band $\mathbf{k}\cdot\mathbf{p}$ models for wurtzite semiconductors require ten parameters that cannot be read directly from the band structure at Γ (anisotropic electron effective mass: 2, Luttinger-like parameters: 6, Nonzero optical matrix parameters: 2) but are easily obtained in the vicinity of Γ from fitting routines readily available in mathematics software packages. A sixteen-band Hamiltonian where energetically higher conduction bands are treated in a similar manner as the basis functions of the eight band model already requires the fitting of 25 parameters. Here, gradient-optimization schemes fail, in particular if a decent fitting throughout the whole Brillouin zone is demanded. A grid-wise search for the optimal parameter set, on the other hand, induces an enormous computational effort. If we assume only ten grid points for each of the 25 parameters, a total of 10^{25} $\mathbf{k}\cdot\mathbf{p}$ band structures would need to be computed and compared to an *ab initio* one – a task which is far beyond nowadays computational resources, even given that

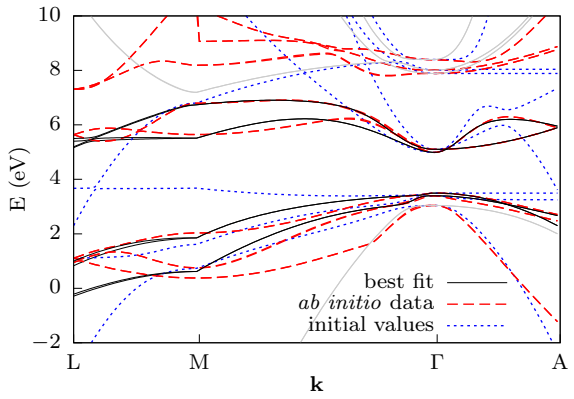

Figure 7: Electronic bandstructure of bulk WZ GaAs obtained from fitting (solid black and gray) a 16-band $\mathbf{k} \cdot \mathbf{p}$ model to a band structure obtained from an *ab initio* calculation (dashed red). Priority was given to the two valence and conduction bands closest to the band gap, respectively (black). The band structure obtained from the initial guess parameter set is shown as dotted blue lines.

this problem can be trivially distributed to a large number of processors.

To overcome this curse of dimensionality, we have implemented a fitting scheme based on stochastic optimization using low-discrepancy point sets [44]. The search intervals of all requested parameters are mapped onto an n-dimensional Sobol sequence [62, 52] of a given length N, thus keeping the number of computed band structures under control while mapping the whole n-dimensional parameter space. The fundamental cost function:

$$v = \sum_{n_{\mathbf{k}}} \mathrm{eig}\left[\hat{H}_{\mathbf{kp}}(P_i) - \epsilon\right]_{i=1..N} \longrightarrow \mathrm{MIN!} \tag{4}$$

with $n_{\mathbf{k}}$ being the number of $\mathbf{k}$ values for which the band structure is sampled, can then be easily modified to optimize additional requirements, e.g. a priorization of selected bands or an improved accuracy of the overall fit in the vicinity of selected high-symmetry points. The scheme is complemented with additional measures to move the whole search range if any of the fit parameters were found to provide the best fit at the boundaries of their respective ranges and provides further optimization of the best-suited sets using gradient optimization and a particle-swarm implementation of a genetic algorithm. An example 16-band $\mathbf{k}\cdot\mathbf{p}$ band structure which has been obtained from fitting a 25-dimensional parameter set to an *ab initio* band structure is shown in Fig. 7, together with the band structure obtained from the initial guess parameter sets. Priority was given to the bottom two conduction and top two valence bands (solid black) in the vicinity of L, M, Γ, and K. The total computational time for this fit, based on a Sobol sequence of N=10000 elements, was about 60 min on a single CPU and the parallel evaluation of a larger set of band structures is a trivial manner. While it is still essential to provide a reasonable initial search range, our approach drastically reduces the computational effort of a parameter fitting process for multiband $\mathbf{k} \cdot \mathbf{p}$ models. Furthermore, the fitting scheme can be initialized with parameter estimates from experiment, theoretical considerations, or existing parameters from comparable materials as a reasonable initial guess.

7 Conclusions

The research in semiconductor nanostructures is largely driven by the experiment. The vast range of nanostructures grown from various material using different growth processes creates a demand for a versatile tool which can predict the electronic properties of such systems with a reasonable accuracy on a daily basis. Our generalized multiband $\mathbf{k}\cdot\mathbf{p}$ scheme represents such a tool, bringing new ideas to the field of $\mathbf{k}\cdot\mathbf{p}$-modelling and thereby overcoming the limits of the decades-old eight-band approach to novel materials and heterostructures classes. Our approach facilitates the possibility to select the Hamiltonian operator and thus the number of bands involved suited best to the system under consideration. This allows to rapidly explore novel materials or unusual heterostructure shapes, where bands beyond the well-established eight-band scheme begin to play a role. In combination with a tool to systematically extract the respective electronic band structure parameters for these more sophisticated models, we establish a work flow from most modern *ab initio* band structure calculations to pioneering device design on the continuum level. The examples presented in this work illustrate the flexibility off our approach and allows us to address very specific questions such as the role of individual donors or the occurence of different crystal phases in nanowire heterostructures without any additional coding being necessary in the software module with high predictive capabilities. The generalized framework allows for rapid prototyping of both novel device concepts as well as new $\mathbf{k}\cdot\mathbf{p}$ models with a highly optimized, computationally efficient gradient minimization that was inspired by the tremendous progress in *ab initio* electronic structure theory of the past decades. Typical calculations can be performed on a standard personal computer or even a laptop within few hours of computational time and do not require high-performance computers that are typically not generally available to experimentalists. Finally, the simplicity of the model and the availability of tutorial videos as well as the possibility to install the software using standard packet managers in most of the common Linux distributions facilitates its applicability for teaching purposes and has been successfully used to excite young students and the general public about the fascinating properties of semiconductor nanostructures.

8 Acknowledgment

This work was funded by the Deutsche Forschungsgemeinschaft (DFG, German Research Foundation) under Germany's Excellence Strategy - EXC2046: MATH+ Berlin Mathematics Research Center (project AA2-5).

References

[1] A. W. Achtstein, O. Marquardt, R. Scott, M. Ibrahim, T. Riedl, A. V. Prudnikau, A. Antanovich, N. Owschimikow, J. K. N. Lindner, M. Artemyev, and U. Woggon. Impact of shell growth on recombination dynamics and exciton-phonon interaction in CdSe-CdS core-shell nanoplatelets. *ACS Nano*, 12(9):9476–9483, 2018. PMID: 30192515.

[2] S. Adachi. *GaAs and Related Materials*. WORLD SCIENTIFIC, 1994.

[3] Y. Aharonov and D. Bohm. Significance of electromagnetic potentials in the quantum theory. *Phys. Rev.*, 115:485–491, Aug 1959.

[4] S. Ahmed, N. Kharche, R. Rahman, M. Usman, S. Lee, H. Ryu, H. Bae, S. Clark, B. Haley, M. Naumov, F. Saied, M. Korkusinski, R. Kennel, M. McLennan, T. B. Boykin, and G. Klimeck. *Multimillion Atom Simulations with Nemo3D*, pages 5745–5783. Springer New York, New York, NY, 2009.

[5] N. Akopian, G. Patriarche, L. Liu, J.-C. Harmand, and V. Zwiller. Crystal phase quantum dots. *Nano Lett.*, 10(4):1198–201, apr 2010.

[6] A. D. Andreev and E. P. O'Reilly. Theory of the electronic structure of GaN/AlN hexagonal quantum dots. *Phys. Rev. B*, 62:15851–15870, Dec 2000.

[7] T. B. Bahder. Erratum: Eight-band $\mathbf{k} \cdot \mathbf{p}$ model of strained zinc-blende crystals [phys. rev. b 41, 11 992 (1990)]. *Phys. Rev. B*, 46:9913–9913, Oct 1992.

[8] G. Bastard. Superlattice band structure in the envelope-function approximation. *Phys. Rev. B*, 24:5693–5697, Nov 1981.

[9] F. Bechstedt and A. Belabbes. Structure, energetics, and electronic states of III-V compound polytypes. *Journal of Physics: Condensed Matter*, 25(27):273201, 2013.

[10] A. Belabbes, C. Panse, J. Furthmüller, and F. Bechstedt. Electronic bands of III-V semiconductor polytypes and their alignment. *Phys. Rev. B*, 86:075208, Aug 2012.

[11] G. Bester. Electronic excitations in nanostructures: an empirical pseudopotential based approach. *Journal of Physics: Condensed Matter*, 21(2):023202, dec 2008.

[12] G. Bester and A. Zunger. Cylindrically shaped zinc-blende semiconductor quantum dots do not have cylindrical symmetry: Atomistic symmetry, atomic relaxation, and piezoelectric effects. *Phys. Rev. B*, 71:045318, Jan 2005.

[13] D. Bimberg. Quantum dot based nanophotonics and nanoelectronics. *Electronics Letters*, 44(3):168–171, 2008.

[14] D. Bimberg, M. Grundmann, and N. Ledentsov. *Quantum Dot Heterostructures*. Wiley, 1999.

[15] M. T. Björk, B. J. Ohlsson, T. Sass, A. I. Persson, C. Thelander, M. H. Magnusson, K. Deppert, L. R. Wallenberg, and L. Samuelson. One-dimensional heterostructures in semiconductor nanowhiskers. *Applied Physics Letters*, 80(6):1058–1060, 2002.

[16] S. Boeck, C. Freysoldt, A. Dick, L. Ismer, and J. Neugebauer. *Computer Phys. Commun.*, 182:543, 2011.

[17] D. Bouwmeester, A. K. Ekert, and A. Zeilinger. *The Physics of Quantum Information: Quantum Cryptography, Quantum Teleportation, Quantum Computation*. Springer Publishing Company, Incorporated, 1st edition, 2010.

[18] M. G. Burt. The justification for applying the effective-mass approximation to microstructures. *Journal of Physics: Condensed Matter*, 4(32):6651–6690, aug 1992.

[19] R. Calarco, M. Marso, T. Richter, A. I. Aykanat, R. Meijers, A. v.d. Hart, T. Stoica, and H. Lüth. Size-dependent photoconductivity in MBE-grown GaN-nanowires. *Nano Letters*, 5(5):981–984, 2005. PMID: 15884906.

[20] A. Canning, L. Wang, A. Williamson, and A. Zunger. Parallel empirical pseudopotential electronic structure calculations for million atom systems. *Journal of Computational Physics*, 160(1):29 – 41, 2000.

[21] T. Cheiwchanchamnangij and W. R. L. Lambrecht. Band structure parameters of wurtzite and zinc-blende GaAs under strain in the GW approximation. *Phys. Rev. B*, 84:035203, Jul 2011.

[22] S. L. Chuang and C. S. Chang. *Phys. Rev. B*, 54:2491, 1996.

[23] B. Chung and M. Gershenzon. The influence of oxygen on the electrical and optical properties of GaN crystals grown by metalorganic vapor phase epitaxy. *Journal of Applied Physics*, 72(2):651–659, 1992.

[24] P. Corfdir, H. Li, O. Marquardt, G. Gao, M. R. Molas, J. K. Zettler, D. van Treeck, T. Flissikowski, M. Potemski, C. Draxl, A. Trampert, S. FernÃąndez-Garrido, H. T. Grahn, and O. Brandt. Crystal-phase quantum wires: One-dimensional heterostructures with atomically flat interfaces. *Nano Letters*, 18(1):247–254, 2018. PMID: 29257698.

[25] P. Corfdir, O. Marquardt, R. B. Lewis, C. Sinito, M. Ramsteiner, A. Trampert, U. Jahn, L. Geelhaar, O. Brandt, and V. M. Fomin. *Advanced Materials*, 31(3):1805645, 2019.

[26] P. Corfdir, J. K. Zettler, C. Hauswald, S. Fernández-Garrido, O. Brandt, and P. Lefebvre. *Phys. Rev. B*, 90:205301, 2014.

[27] A. De and C. E. Pryor. Predicted band structures of III-V semiconductors in the wurtzite phase. *Phys. Rev. B*, 81:155210, Apr 2010.

[28] M. Ehrhardt and T. Koprucki. *Multi-Band Effective Mass Approximations: Advanced Mathematical Models and Numerical Techniques*. Lecture Notes in Computational Science and Engineering. Springer International Publishing, 2014.

[29] L. A. T. Greif, S. T. Jagsch, M. R. Wagner, and A. Schliwa. Tuning the emission directionality of stacked quantum dots. *ACS Photonics*, 5(12):4838–4845, 2018.

[30] P. D. Hodgson, M. Bentley, E. Delli, R. Beanland, M. C. Wagener, J. R. Botha, and P. J. Carrington. Optical and structural properties of InGaSb/GaAs quantum dots grown by molecular beam epitaxy. *Semiconductor Science and Technology*, 33(12):125021, nov 2018.

[31] M. J. Holmes, K. Choi, S. Kako, M. Arita, and Y. Arakawa. Room-temperature triggered single photon emission from a III-Nitride site-controlled nanowire quantum dot. *Nano Letters*, 14(2):982–986, 2014. PMID: 24422516.

[32] J.-M. Jancu, R. Scholz, E. A. de Andrada e Silva, and G. C. La Rocca. Atomistic spin-orbit coupling and $\mathbf{k} \cdot \mathbf{p}$ parameters in III-V semiconductors. *Phys. Rev. B*, 72:193201, Nov 2005.

[33] V. M. Kaganer and A. Y. Belov. Strain and x-ray diffraction from axial nanowire heterostructures. *Phys. Rev. B*, 85:125402, Mar 2012.

[34] A. Kaur and U. Gupta. A review on applications of nanoparticles for the preconcentration of environmental pollutants. *J. Mater. Chem.*, 19:8279–8289, 2009.

[35] K. Kawasaki, D. Yamazaki, A. Kinoshita, H. Hirayama, K. Tsutsui, and Y. Aoyagi. GaN quantum-dot formation by self-assembling droplet epitaxy and application to single-electron transistors. *Applied Physics Letters*, 79(14):2243–2245, 2001.

[36] R. W. Keyes. The effect of randomness in the distribution of impurity atoms on FET thresholds. *Appl. Phys.*, 8:251–259, Nov 1975.

[37] M. Kibria, F. Chowdhury, S. Zhao, B. AlOtaibi, M. L. Trudeau, H. Guo, and Z. Mi. Visible light-driven efficient overall water splitting using p-type metal-nitride nanowire arrays. *Nature Communications*, 6:6797, 2015.

[38] A. Kikuchi, M. Kawai, M. Tada, and K. Kishino. InGaN/GaN multiple quantum disk nanocolumn light-emitting diodes grown on (111) si substrate. *Japanese Journal of Applied Physics*, 43(No. 12A):L1524–L1526, nov 2004.

[39] P. Klenovský, A. Schliwa, and D. Bimberg. Electronic states of (In,Ga)(As,Sb)/GaAs/GaP quantum dots. *Phys. Rev. B*, 100:115424, Sep 2019.

[40] S. Li and A. Waag. GaN based nanorods for solid state lighting. *Journal of Applied Physics*, 111(7):071101, 2012.

[41] W. Lu and C. M. Lieber. Semiconductor nanowires. *Journal of Physics D: Applied Physics*, 39(21):R387–R406, oct 2006.

[42] O. Marquardt, S. Boeck, C. Freysoldt, T. Hickel, and J. Neugebauer. Plane-wave implementation of the real-space $\mathbf{k} \cdot \mathbf{p}$ formalism and continuum elasticity theory. *Computer Physics Communications*, 181(4):765 – 771, 2010.

[43] O. Marquardt, S. Boeck, C. Freysoldt, T. Hickel, S. Schulz, J. Neugebauer, and E. P. O'Reilly. *Comp. Mat. Sci.*, 95:280, 2014.

[44] O. Marquardt, M. A. Caro, T. Koprucki, P. Mathé, and M. Willatzen. Multiband $\mathrm{k} \cdot \mathrm{p}$ model and fitting scheme for ab initio based electronic structure parameters for wurtzite gaas. *Phys. Rev. B*, 101:235147, Jun 2020.

[45] O. Marquardt, L. Geelhaar, and O. Brandt. Minimizing the impact of surface potentials in axial $\mathrm{In}_x\mathrm{Ga}_{1-x}\mathrm{N}$/GaN nanowire heterostructures by reducing their diameter. *Journal of Physics D: Applied Physics*, 47(39):394007, sep 2014.

[46] O. Marquardt, L. Geelhaar, and O. Brandt. *Nano Lett.*, 15:4289, 2015.

[47] O. Marquardt, C. Hauswald, M. Wölz, L. Geelhaar, and O. Brandt. *Nano Lett.*, 13:3298, 2013.

[48] O. Marquardt, M. Ramsteiner, P. Corfdir, L. Geelhaar, and O. Brandt. *Phys. Rev. B*, 95:245309, 2017.

[49] S. Mokkapati and C. Jagadish. III-V compound SC for optoelectronic devices. *Materials Today*, 12(4):22 – 32, 2009.

[50] W. J. Moore, J. A. Freitas, G. C. B. Braga, R. J. Molnar, S. K. Lee, K. Y. Lee, and I. J. Song. Identification of Si and O donors in hydride-vapor-phase epitaxial GaN. *Applied Physics Letters*, 79(16):2570–2572, 2001.

[51] S. Nakamura and G. Fasol. *The Blue Laser Diode: GaN Based Light Emitters and Lasers*. Physics and Astronomy. Springer, 1997.

[52] H. Niederreiter. *Random Number Generation and quasi-Monte Carlo Methods*. Society for Industrial and Applied Mathematics, 1992.

[53] P. Pfeffer and W. Zawadzki. Five-level $\mathbf{k}\cdot\mathbf{p}$ model for the conduction and valence bands of GaAs and InP. *Phys. Rev. B*, 53:12813–12828, May 1996.

[54] C. Pryor. Eight-band calculations of strained InAs/GaAs quantum dots compared with one-, four-, and six-band approximations. *Phys. Rev. B*, 57:7190–7195, Mar 1998.

[55] C. E. Pryor and M.-E. Pistol. Atomistic $\mathbf{k}\cdot\mathbf{p}$ theory. *Journal of Applied Physics*, 118(22):225702, 2015.

[56] E. Ribeiro, A. O. Govorov, W. Carvalho, and G. Medeiros-Ribeiro. Aharonov-Bohm Signature for Neutral Polarized Excitons in Type-II Quantum Dot Ensembles. *Phys. Rev. Lett.*, 92:126402, Mar 2004.

[57] T. Saito and Y. Arakawa. Electronic structure of piezoelectric $In_{0.2}Ga_{0.8}N$ quantum dots in GaN calculated using a tight-binding method. *Physica E: Low-dimensional Systems and Nanostructures*, 15(3):169 – 181, 2002.

[58] N. Sano and M. Tomizawa. Random dopant model for three-dimensional drift-diffusion simulations in metal-oxide-semiconductor field-effect-transistors. *Applied Physics Letters*, 79(14):2267–2269, 2001.

[59] R. Santoprete, B. Koiller, R. B. Capaz, P. Kratzer, Q. K. K. Liu, and M. Scheffler. Tight-binding study of the influence of the strain on the electronic properties of InAs/GaAs quantum dots. *Phys. Rev. B*, 68:235311, Dec 2003.

[60] S. Schulz and G. Czycholl. Tight-binding model for semiconductor nanostructures. *Phys. Rev. B*, 72:165317, Oct 2005.

[61] G. Signorello, E. Lörtscher, P. A. Khomyakov, S. Karg, D. L. Dheeraj, B. Gotsmann, H. Weman, and H. Riel. Inducing a direct-to-pseudodirect bandgap transition in wurtzite GaAs nanowires with uniaxial stress. *Nature Comm.*, 5:3655, Apr 2014.

[62] I. M. Sobol. *Zh. Vych. Mat. Mat. Fiz.*, 7:784, 1967.

[63] I. P. Soshnikov, G. E. Cirlin, A. A. Tonkikh, Y. B. Samsonenko, V. G. Dubovskii, V. M. Ustinov, O. M. Gorbenko, D. Litvinov, and D. Gerthsen. Atomic structure of MBE-grown GaAs nanowhiskers. *Phys. Solid State*, 47:2213–2218, Dec 2005.

[64] O. Stier, M. Grundmann, and D. Bimberg. Electronic and optical properties of strained quantum dots modeled by 8-band $\mathbf{k}\cdot\mathbf{p}$ theory. *Phys. Rev. B*, 59:5688–5701, Feb 1999.

[65] S. Tomić and N. Vukmirović. Symmetry reduction in multiband hamiltonians for semiconductor quantum dots: The role of interfaces and higher energy bands. *Journal of Applied Physics*, 110(5):053710, 2011.

[66] R. G. Veprek, S. Steiger, and B. Witzigmann. Reliable $\mathbf{k}\cdot\mathbf{p}$ band structure calculation for nanostructures using finite elements. *Journal of Computational Electronics*, 7:521–529, oct 2008.

[67] I. Vurgaftman, J. R. Meyer, and L. R. Ram-Mohan. *J. Appl. Phys.*, 89:5815, 2001.

[68] P. Waltereit, O. Brandt, A. Trampert, H. T. Grahn, J. Menninger, M. Ramsteiner, K. Reiche, and K. Ploog. Nitride semiconductors free of electrostatic fields for efficient white light-emitting diodes. *Nature*, 406:865–868, 2000.

[69] L.-W. Wang, J. Kim, and A. Zunger. Electronic structures of [110]-faceted self-assembled pyramidal InAs/GaAs quantum dots. *Phys. Rev. B*, 59:5678–5687, Feb 1999.

[70] L. W. Wang, A. J. Williamson, A. Zunger, H. Jiang, and J. Singh. Comparison of the $\mathbf{k} \cdot \mathbf{p}$ and direct diagonalization approaches to the electronic structure of InAs/GaAs quantum dots. *Applied Physics Letters*, 76(3):339–341, 2000.

[71] M. Winkelnkemper, A. Schliwa, and D. Bimberg. *Phys. Rev. B*, 74:155322, 2006.

[72] M. Wölz, J. Lähnemann, O. Brandt, V. M. Kaganer, M. Ramsteiner, C. Pfüller, C. Hauswald, C. N. Huang, L. Geelhaar, and H. Riechert. Correlation between In content and emission wavelength of $\mathrm{In}_x\mathrm{Ga}_{1-x}$N/GaN nanowire heterostructures. *Nanotechnology*, 23(45):455203, oct 2012.

[73] X. Yuan, F. Weyhausen-Brinkmann, J. Martín-Sánchez, G. Piredda, V. Křápek, Y. Huo, H. Huang, C. Schimpf, O. G. Schmidt, J. Edlinger, G. Bester, R. Trotta, and A. Rastelli. Uniaxial stress flips the natural quantization axis of a quantum dot for integrated quantum photonics. *Nature Comm.*, 9:3058, 2018.

[74] I. Zardo, S. Conesa-Boj, F. Peiro, J. R. Morante, J. Arbiol, E. Uccelli, G. Abstreiter, and A. Fontcuberta i Morral. Raman spectroscopy of wurtzite and zinc-blende GaAs nanowires: Polarization dependence, selection rules, and strain effects. *Phys. Rev. B*, 80:245324, Dec 2009.

[75] Y. Zhao, S. Tanaka, C. C. Pan, K. Fujito, D. Feezell, J. S. Speck, S. P. DenBaars, and S. Nakamura. *Appl. Phys. Express*, 4:082104, 2011.

[76] W. Zhou and J. J. Coleman. Semiconductor quantum dots. *Current Opinion in Solid State and Materials Science*, 20(6):352 – 360, 2016. the COSSMS Twentieth Anniversary Issue.

[77] A. Zrenner, E. Beham, S. Stufler, F. Findeis, M. Bichler, and G. Abstreiter. Coherent properties of a two-level system based on a quantum-dot photodiode. *Nature*, 418:612–614, 2002.